

Asymmetry of the parallel momentum distribution of (p, pN) reaction residues

Kazuyuki Ogata,^{1,*} Kazuki Yoshida,¹ and Kosho Minomo¹

¹Research Center for Nuclear Physics (RCNP), Osaka University, Ibaraki 567-0047, Japan

(Dated: July 4, 2018)

The parallel momentum distribution (PMD) of the residual nuclei of the $^{14}\text{O}(p, pn)^{13}\text{O}$ and $^{14}\text{O}(p, 2p)^{13}\text{N}$ reactions at 100 and 200 MeV/nucleon in inverse kinematics is investigated with the framework of the distorted wave impulse approximation. The PMD shows an asymmetric shape characterized by a steep fall-off on the high momentum side and a long-ranged tail on the low momentum side. The former is found to be due to the phase volume effect reflecting the energy and momentum conservation, and the latter is to the momentum shift of the outgoing two nucleons inside an attractive potential caused by the residual nucleus. Dependence of these effects on the nucleon separation energy of the projectile and the incident energy is also discussed.

PACS numbers: 24.10.Eq, 25.60.Gc, 25.40.-h

I. INTRODUCTION

The single-particle (s.p.) nature is one of the most important properties of nuclei. Since 90's, triggered by the invention of radioactive isotope (RI) beam technology, intensive studies on the s.p. structure of unstable nuclei have been done; see, for a review, Ref. [1]. Many experiments of one- or two-nucleon removal processes were performed [2–16] and the parallel momentum distribution (PMD) of the residual nucleus B has widely been used to determine the s.p. structure of the incident particle A, i.e., the orbital angular momentum, the s.p. energy, and the spectroscopic factor of the nucleon(s) inside the nucleus A.

The removal reaction does not specify the final state of the target nucleus T, and it is not trivial to apply a direct reaction theory to such an inclusive process. The Glauber model [17–20] is one of the most successful models to study the nucleon removal process; the eikonal and adiabatic approximations allow one to treat the scattering of each constituent of A off T separately, and the generalized unitarity of the scattering matrix elements of the removed nucleon(s) gives a simple form of reaction observables for the nucleon removal process. Recently, the eikonal reaction theory (ERT) [21] was developed as an extension of the continuum-discretized coupled-channels method (CDCC) [22–24]. Although ERT has successfully been applied to one- and two-neutron removal processes [25], formulation of the PMD and differential cross sections with the ERT has not been completed.

Despite the great success of the Glauber model in extracting s.p. information on unstable nuclei from reaction data, the shape of the PMD calculated with the Glauber model is restricted to being symmetric. On the other hand, in some cases the observed PMD shows quite large asymmetry [7, 9, 11]. Although this does not necessarily cause ambiguity of the s.p. information extracted by the Glauber model, as discussed in Ref. [11], it will be interesting and important to clarify the mechanism of the asymmetry of the PMD. It should be remarked that recently the transfer to the continuum (TC)

method [26, 27] was applied to the one-neutron removal process from ^{14}O by ^9Be at 53 MeV/nucleon and reproduced quite well the asymmetric shape of the PMD [28]. At this moment, the TC method is restricted to neutron removal processes.

As mentioned, it is difficult to describe an inclusive process, to which huge numbers of the final states of T contribute. On the other hand, the description of elastic breakup (EB), in which T stays in the ground state in the final channel, is well established. CDCC [22–24], the dynamical eikonal approximation (DEA) [29, 30], the Faddeev–Alt-Grassberger-Sandhas (Faddeev-AGS) theory [31, 32] etc. can be adopted; CDCC is even applicable to the nuclear and Coulomb breakup of a three-body projectile by a target nucleus [33–36].

The asymmetry of the PMD, its EB component in particular, of ^{14}C after the one-neutron removal from ^{15}C by ^9Be at 54 MeV/nucleon was discussed in Ref. [37] by means of CDCC. It was concluded that the accurate treatment of three-body reaction dynamics was essential to reproduce the asymmetry of the PMD of ^{14}C . Because of this finding, sometimes the asymmetry of a PMD is regarded as a result of higher-order effects. Discussion on the very large asymmetry found in $^9\text{Be}(^{46}\text{Ar}, ^{45}\text{Ar } x)$, where x indicates that all other particles are not detected, at 70 MeV/nucleon [11], however, has not been done.

In the present study, we focus on one-nucleon knockout processes by a hydrogen target, i.e., (p, pN) reactions in inverse kinematics, in which only the EB process occurs. (p, pN) reactions have been used to determine the s.p. structure of nuclei; for reviews, see Refs. [38–40]. An important feature of (p, pN) reactions is that the energy and momentum transfer (ω - q) as well as the angular momentum transfer Δl is large in general. This makes the reaction mechanism rather simple, and the distorted-wave impulse approximation (DWIA) has been successful in describing (p, pN) reaction observables. Recently, a comparison between the DWIA and the Faddeev-AGS theory was done for $^{11}\text{Be}(p, pn)^{10}\text{Be}$ and $^{12}\text{C}(p, pn)^{11}\text{B}$, and the results of the two methods were shown to agree very well with each other at proton energies above 100 MeV [41, 42]. It should be noted that the Glauber model [17–20], which relies on the adiabatic approximation, assumes small ω - q and is thus not suitable for describing (p, pN) reactions. CDCC does not use the adiabatic approxi-

*kazuyuki@rcnp.osaka-u.ac.jp

mation and is applicable to (p, pN) reactions [43–45]. However, the model space of CDCC required to describe (p, pN) reactions is large mainly because of the large value of Δl . Furthermore, for a knockout process of a tightly bound nucleon, ω - q and Δl are even larger, which will make CDCC unpractical.

In this paper we investigate the asymmetry of the PMD of $^{14}\text{O}(p, pN)$ reactions in inverse kinematics at 100 and 200 MeV/nucleon. ^{14}O has the neutron and proton separation energies of 23.2 MeV and 4.63 MeV, respectively, and their large difference is expected to give a quite different shape to the PMD of the reaction residues, i.e., ^{13}O and ^{13}N . The main purpose of the present study is to understand the mechanism that gives the asymmetric shape of the PMD. We adopt the DWIA with the eikonal approximation, the accuracy of which is judged by comparison with the experimental data of the triple differential cross section (TDX) of $^{12}\text{C}(p, pN)^{11}\text{B}$ at 392 MeV [46]. Roles of the phase volume, which guarantees the energy and momentum conservation, and the distortion of the outgoing two nucleons by the residual nucleus are investigated separately. Quite recently, in Ref. [47] an eikonal DWIA model was developed for describing the momentum distribution (MD) of (p, pN) reaction residues. The authors focused on reactions at around 500 MeV/nucleon, and the asymmetry of the PMD, which is expected to appear at lower energies, has not been discussed.

The construction of this paper is as follows. In Sec. II formulation of the TDX and PMD with the eikonal DWIA is given. In Sec. III first we show the accuracy of the eikonal DWIA by comparing the result of the TDX of $^{12}\text{C}(p, pN)^{11}\text{B}$ at 392 MeV with experimental data. We then show the PMD of the $^{14}\text{O}(p, pN)$ reaction residues at 100 MeV/nucleon. The phase volume effect on the high momentum side and the distortion effect on the low momentum side are discussed in detail. Results at 200 MeV/nucleon are also investigated. Finally, we give a summary in Sec. IV.

II. FORMALISM

We consider $A(p, 2p)B$ and $A(p, pn)B$ reactions in inverse or normal kinematics. We adopt the framework of the DWIA to calculate the TDX and the PMD. Both observables are evaluated in the frame in which A is at rest, i.e., the A-rest frame. We refer to the proton in the initial channel as particle 0, and the outgoing two nucleons to as particle 1 and 2. The momentum (in the unit of \hbar) and the total energy of particle i ($= 0, 1, 2$, or B) are denoted by \mathbf{K}_i and E_i , respectively; T_i represents the kinetic part of E_i and Ω_i is the solid angle of \mathbf{K}_i . These quantities with and without the superscript A mean that they are evaluated in the A-rest frame and the p -A center-of-mass (c.m.) frame, respectively. In the following equations, we adopt the relativistic kinematics for each particle, i.e., $E_i^A = \sqrt{(m_i c^2)^2 + (\hbar c K_i^A)^2}$ and $E_i = \sqrt{(m_i c^2)^2 + (\hbar c K_i)^2}$, with m_i the rest mass of particle i , are used. The Lorentz transformation is adopted to relate the four-dimensional momenta ($\hbar \mathbf{K}_i^A$, E_i^A/c) and ($\hbar \mathbf{K}_i$, E_i/c).

The antisymmetrization between particles 1 and 2 is under-

stood to be taken into account in the nucleon-nucleon (NN) transition matrix t_{NN} , which is treated approximately by using

$$\frac{(m_N/2)^2}{(2\pi\hbar^2)^2} |t_{NN}|^2 \approx \bar{\sigma}_{NN}. \quad (1)$$

The nucleon mass is denoted by m_N and $\bar{\sigma}_{NN}$ is the NN elastic differential cross section averaged over incident energies and scattering angles relevant to the knockout process considered. Equation (1) is in fact based on the following three approximations. First, t_{NN} is evaluated with the NN asymptotic kinematics [48]. Second, the off-the-energy-shell t_{NN} in the nuclear medium is approximated by an averaged on-shell matrix element in free space. Then one can evaluate $|t_{NN}|^2$ by the NN differential cross section multiplied by a kinetic constant. Third, we take an average of the NN differential cross section to have a one number $\bar{\sigma}_{NN}$ to be used in the calculation of the knockout process. Note that $\bar{\sigma}_{NN}$ depends on the reaction type, i.e., $(p, 2p)$ or (p, pn) , and the incident energy of the knockout process. These rather drastic approximations to t_{NN} are examined by comparing the calculated TDX with experimental data in Sec. III B.

We make the eikonal approximation to the distorted waves of particles 0, 1, and 2, as in Ref. [47]; we further approximate the eikonal wave function with the forward scattering assumption; see Eqs. (8) and (9) below.

The TDX is then given by

$$\frac{d^3\sigma}{dE_1^A d\Omega_1^A d\Omega_2^A} = F_{\text{kin}} C_0 \sum_m \bar{\sigma}_{NN} (2\pi)^2 \left| \bar{T}_{\mathbf{K}_N, K_0 K_1 K_2}^{nljm} \right|^2, \quad (2)$$

where

$$F_{\text{kin}} \equiv J_A \frac{K_1 K_2 E_1 E_2}{\hbar^4 c^4} \left[1 + \frac{E_2}{E_B} + \frac{E_2}{E_B} \frac{\mathbf{K}_1 \cdot \mathbf{K}_2}{K_2^2} \right]^{-1} \quad (3)$$

with J_A the Jacobian for the transformation from the p -A c.m. frame to the A-rest frame, and

$$C_0 = \frac{E_0^A}{(\hbar c)^2 K_0^A} \frac{1}{(2l+1)} \frac{4\hbar^4}{(2\pi)^3 m_N^2}. \quad (4)$$

The reduced transition amplitude is given by

$$\begin{aligned} \bar{T}_{\mathbf{K}_N, K_0 K_1 K_2}^{nljm} &= \int db b J_m(K_N b) dz e^{-iK_N z} \\ &\times F_{K_0 K_1 K_2}(b, z) \varphi_{nlj}(R) \bar{P}_{lm}(\cos\theta_R), \end{aligned} \quad (5)$$

where n , l , and j are, respectively, the principal quantum number, the orbital angular momentum, and the total spin of the s.p. orbit of the nucleon in A; m is the third component of j . φ_{nlj} is the radial part of the s.p. wave function, and \bar{P}_{lm} is defined through the spherical harmonics Y_{lm} by

$$\bar{P}_{lm}(\cos\theta_R) = Y_{lm}(\hat{\mathbf{R}}) e^{-im\phi_R}, \quad (6)$$

where $\hat{\mathbf{R}}$, θ_R , and ϕ_R are the solid, polar, and azimuthal angles of \mathbf{R} , respectively. The z -axis is taken to be the direction

of the incident particle, i.e., p (A) in normal (inverse) kinematics, and b is the length of the projected vector \mathbf{b} of \mathbf{R} on the plane perpendicular to the z -axis. J_m is the Bessel function of the first kind.

The missing momentum \mathbf{K}_N that plays a central role in (p, pN) reactions is defined by

$$\begin{aligned} \mathbf{K}_N &= \mathbf{K}_1 + \mathbf{K}_2 - \frac{A-1}{A}\mathbf{K}_0 = -\mathbf{K}_B - \frac{A-1}{A}\mathbf{K}_0 \\ &\equiv K_{Nz}\mathbf{e}_z + K_{Nb}\mathbf{e}_b, \end{aligned} \quad (7)$$

where A is the mass number of A and \mathbf{e}_z (\mathbf{e}_b) is the unit vector for the direction of z (\mathbf{b}). It should be noted that with high accuracy one can find $\mathbf{K}_N \approx -\mathbf{K}_B^A$. If B is assumed to be a spectator in the (p, pN) process, \mathbf{K}_N can therefore be interpreted as the momentum of the struck nucleon in the A-rest frame before the NN collision.

In the present eikonal DWIA, the distortion effects for particle 0, 1, and 2 are aggregated into the so-called distorted-wave factor $F_{K_0K_1K_2}$ given by

$$\begin{aligned} F_{K_0K_1K_2}(b, z) &= \exp\left[\frac{1}{i\hbar v_0} \int_{-\infty}^z U_0(b, z') dz'\right] \\ &\times \exp\left[\frac{1}{i\hbar v_1} \int_z^{\infty} U_1(b, z') dz'\right] \\ &\times \exp\left[\frac{1}{i\hbar v_2} \int_z^{\infty} U_2(b, z') dz'\right] \end{aligned} \quad (8)$$

in normal kinematics and by

$$\begin{aligned} F_{K_0K_1K_2}(b, z) &= \exp\left[\frac{1}{i\hbar v_0} \int_z^{\infty} U_0(b, z') dz'\right] \\ &\times \exp\left[\frac{1}{i\hbar v_1} \int_{-\infty}^z U_1(b, z') dz'\right] \\ &\times \exp\left[\frac{1}{i\hbar v_2} \int_{-\infty}^z U_2(b, z') dz'\right] \end{aligned} \quad (9)$$

in inverse kinematics. U_i ($i = 0, 1, 2$) is the distorting potential for particle i and v_i is its velocity.

The MD of B is defined by

$$\begin{aligned} \frac{d\sigma}{d\mathbf{K}_B^A} &= C_0 \int d\mathbf{K}_1^A d\mathbf{K}_2^A \eta_{M\phi}^A \delta(E_f^A - E_i^A) \delta(\mathbf{K}_f^A - \mathbf{K}_i^A) \\ &\times \bar{\sigma}_{NN} \sum_m (2\pi)^2 \left| \bar{T}_{\mathbf{K}_N, K_0K_1K_2}^{nljm} \right|^2, \end{aligned} \quad (10)$$

where

$$\eta_{M\phi}^A = \frac{E_1 E_2 E_B}{E_1^A E_2^A E_B^A}. \quad (11)$$

The total energy (momentum) of the reaction system in the A-rest frame in the initial and final channels is denoted by E_i^A (\mathbf{K}_i^A) and E_f^A (\mathbf{K}_f^A), respectively. Equation (10) can be reduced to

$$\begin{aligned} \frac{d\sigma}{d\mathbf{K}_B^A} &= C_0 \frac{1}{(\hbar c)^2 Q^A} \int dK_1^A K_1^A E_2^A d\varphi_{1Q}^A \eta_{M\phi}^A \\ &\times \bar{\sigma}_{NN} \sum_m (2\pi)^2 \left| \bar{T}_{\mathbf{K}_N, K_0K_1K_2}^{nljm} \right|^2, \end{aligned} \quad (12)$$

where \mathbf{K}_2^A is understood to be fixed at $\mathbf{K}_0^A - \mathbf{K}_1^A - \mathbf{K}_B^A$ by the momentum conservation. We measure the solid angle of particle 1 with respect to $\mathbf{Q}^A \equiv \mathbf{K}_0^A - \mathbf{K}_B^A$ as

$$d\mathbf{K}_1^A = (K_1^A)^2 dK_1 d(\cos\theta_{1Q}^A) d\varphi_{1Q}^A. \quad (13)$$

In Eq. (12) $\cos\theta_{1Q}^A$ has been fixed at a value that satisfies the energy conservation; this value as well as the lower and upper limits of K_1^A is given analytically. The PMD is given by integrating the MD over the absolute value of the b component of \mathbf{K}_B^A :

$$\frac{d\sigma}{dK_B^A} = \int dK_{Bb}^A K_{Bb}^A \frac{d\sigma}{d\mathbf{K}_B^A}. \quad (14)$$

When the theory is compared with PMD data integrated over the azimuthal angle of \mathbf{K}_B^A , Eq. (14) must be multiplied by 2π . For reactions in inverse kinematics, the A-rest frame is different from the laboratory frame (L-frame). Then

$$\frac{d\sigma}{d\mathbf{K}_B^L} = \frac{E_B^A}{E_B^L} \frac{d\sigma}{d\mathbf{K}_B^A} \quad (15)$$

can be used for comparison with experimental data, if necessary. The superscript L indicates the L-frame.

If plane wave impulse approximation (PWIA) is adopted, further simplification of Eq. (12) can be done:

$$\frac{d\sigma^{\text{PW}}}{d\mathbf{K}_B^A} = \bar{\rho}_{\mathbf{K}_B^A} \tilde{\mathfrak{F}}_{\mathbf{K}_B^A}, \quad (16)$$

where the phase volume $\bar{\rho}_{\mathbf{K}_B^A}$ is given by

$$\bar{\rho}_{\mathbf{K}_B^A} = \frac{1}{(\hbar c)^2 Q^A} \int dK_1^A K_1^A E_2^A d\varphi_{1Q}^A \eta_{M\phi}^A \quad (17)$$

and the effective s.p. MD is defined by

$$\tilde{\mathfrak{F}}_{\mathbf{K}_B^A} = C_0 \bar{\sigma}_{NN} \sum_m \left| \tilde{\phi}_{nljm}(\mathbf{K}_N) \right|^2 \quad (18)$$

with

$$\tilde{\phi}_{nljm}(\mathbf{K}_N) = \int d\mathbf{R} e^{-i\mathbf{K}_N \cdot \mathbf{R}} \varphi_{nlj}(R) Y_{lm}(\hat{\mathbf{R}}). \quad (19)$$

Thus $\bar{\rho}_{\mathbf{K}_B^A}$ and $\tilde{\mathfrak{F}}_{\mathbf{K}_B^A}$ are factorized. Equations (16)–(19) are used in Sec. III C to see the phase volume effect on the PMD.

In the actual calculation Eq. (17) is used, i.e., the energy and momentum conservation based on the relativistic kinematics is taken into account. For an interpretation of the numerical result, however, the following nonrelativistic expression of $\bar{\rho}_{\mathbf{K}_B^A}$ will be helpful:

$$\bar{\rho}_{\mathbf{K}_B^A}^{\text{NR}} \equiv \frac{\pi m_N}{\hbar^2} \sqrt{(\mathbf{K}_0^A + \mathbf{K}_B^A)^2 - \frac{2A}{A-1} (K_B^A)^2 - \bar{S}_N}, \quad (20)$$

where $\bar{S}_N \equiv 4m_N S_N / \hbar^2$ with S_N the nucleon separation energy of A. Although it is rather trivial, the argument of the square root in Eq. (20) is understood to be not negative; this condition determines, within the nonrelativistic kinematics, the allowed region of \mathbf{K}_B^A for satisfying the energy and momentum conservation. A similar discussion can be done in the relativistic kinematics. However, the functional form of $\bar{\rho}_{\mathbf{K}_B^A}$ is much more complicated than Eq. (20).

III. RESULTS AND DISCUSSION

A. Numerical inputs

We use the s.p. potential of Bohr and Mottelson [49] for the nucleon inside the nucleus. The depth of its central part is changed so as to reproduce S_N . For the nucleon distorting potential below (above) 200 MeV, we adopt the parameter set of Koning and Delaroche [50] (Dirac phenomenology [51]); its energy dependence is explicitly taken into account. We multiply each of the distorted waves by the Perey factor [52] $F_{\text{Per}}(R) = [1 - \mu\beta^2/(2\hbar^2)U(R)]^{-1/2}$, where μ is the reduced mass between the scattering two particles, to include the effect of the nonlocality of the distorting potential; the range β of nonlocality is chosen to be 0.85 fm. The parametrization of Franey and Love [53] for t_{NN} is used.

B. TDX and PMD calculated with eikonal DWIA

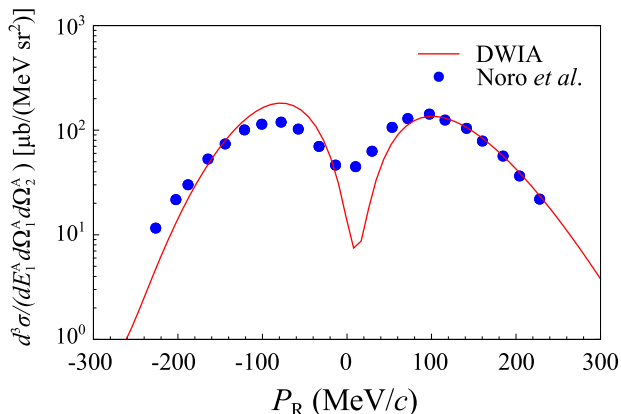


FIG. 1: (Color online) Triple differential cross section for the $^{12}\text{C}(p, 2p)^{11}\text{B}$ reaction at 392 MeV in normal kinematics. The definition of the horizontal axis and detailed kinematical conditions for the outgoing protons are given in the text. The experimental data are taken from Ref. [46].

First we test the accuracy of the eikonal DWIA model described in Sec. II. We calculate the TDX for the $^{12}\text{C}(p, 2p)^{11}\text{B}$ reaction at 392 MeV in normal kinematics with Eq. (2). We follow the Madison convention and the kinematics of the outgoing two protons is fixed as $T_1 = 250$ (MeV), $\theta_1 = 32.5^\circ$, $\phi_1 = 0^\circ$, and $\phi_2 = 180^\circ$; this means that the energy transfer $\hbar\omega$ is 142 MeV and the momentum transfer q is 2.59 fm^{-1} . We assume that the $0p3/2$ proton in ^{12}C is knocked out. In Fig. 1 we show the result of the TDX and the experimental data [46]. We use the spectroscopic factor $\mathcal{S} = 1.72$ determined by the $(e, e'p)$ experiment [54]. The horizontal axis is defined by

$$P_R = \hbar K_B^A \frac{K_{Bz}^A}{|K_{Bz}^A|}. \quad (21)$$

One sees the calculation reproduces the data very well, which suggests the success of the present reaction model, i.e., the eikonal DWIA with the forward scattering assumption and the use of the averaged NN cross section in free space. It should be noted that the undershooting at around $P_R = 0$, which corresponds to the so-called quasi-free condition (QFC), is mainly because the experimental data have been integrated over $d\Omega_1^A$ and $d\Omega_2^A$ in the range of the resolution of the detectors [46]. The calculated TDX reproduces the data up to $|P_R| \sim 200 \text{ MeV}/c$, i.e., well away from the QFC point. This will be due in part to the kinematical condition corresponding to large $\omega - q$.

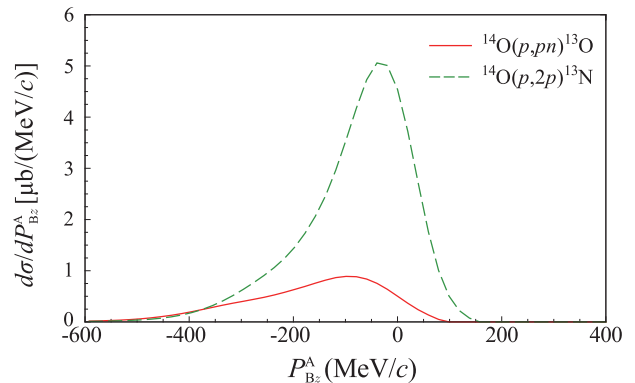


FIG. 2: (Color online) Parallel momentum distribution of the $^{14}\text{O}(p, pn)^{13}\text{O}$ (solid line) and $^{14}\text{O}(p, 2p)^{13}\text{N}$ (dashed line) reaction residues at 100 MeV/nucleon in inverse kinematics.

Next we show in Fig. 2 the PMD of the residual nuclei of the $^{14}\text{O}(p, pn)$ (solid line) and $^{14}\text{O}(p, 2p)$ (dashed line) reactions at 100 MeV/nucleon, as a function of $P_{Bz}^A = \hbar K_{Bz}^A$. For the former (latter) the $0p3/2$ neutron ($0p1/2$ proton) with $S_N = 23.2$ MeV (4.63 MeV) is assumed to be knocked out by the target proton; from now on we always use $\mathcal{S} = 1$. In both reactions the PMD shows clear asymmetry. For more quantitative discussion, we divide the FWHM Γ into two parts corresponding to the low (Γ_L) and high (Γ_H) momentum sides with respect to the peak position P_{cen} :

$$\Gamma = \Gamma_L + \Gamma_H. \quad (22)$$

The asymmetry A_Γ is defined by Γ_L/Γ_H . The values of P_{cen} ,

TABLE I: P_{cen} , Γ , Γ_L , Γ_H , and A_Γ for the $^{14}\text{O}(p, pN)$ reaction residues at 100 MeV/nucleon.

nucleus	P_{cen} (MeV/c)	Γ (MeV/c)	Γ_L (MeV/c)	Γ_H (MeV/c)	A_Γ
^{13}O	-92	266	182	84	2.17
^{13}N	-31	178	104	74	1.41

Γ , Γ_L , Γ_H , and A_Γ are listed in Table I. One sees that the shift of the peak position from the origin, $|P_{\text{cen}}|$, of ^{13}O is three times as large as that of ^{13}N . Another finding is that the two residues have similar values of Γ_H , whereas Γ_L of them are quite different from each other. In Secs. III C and III D we investigate these features of the PMD in more detail.

C. Phase volume effect on the high momentum side

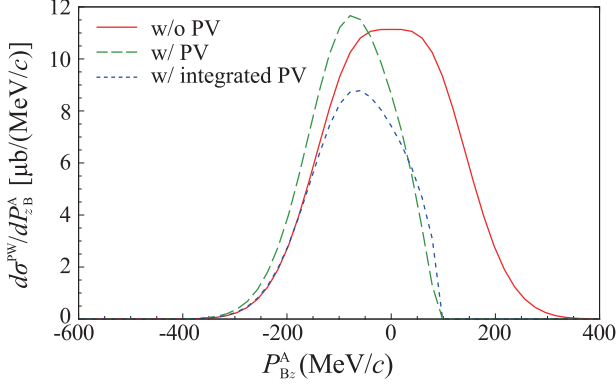


FIG. 3: (Color online) Parallel momentum distribution of the $^{14}\text{O}(p, pn)^{13}\text{O}$ reaction residue at 100 MeV/nucleon in inverse kinematics. The solid (dashed) line shows the result of the PWIA without (with) taking into account the phase volume. The dotted line is the same as the dashed line but an averaged phase volume is used (see the text for detail).

It is quite well known that the PMD on the high momentum side is affected by the energy conservation, the effect of which on the PMD is expressed by the phase volume $\bar{\rho}_{K_B^A}$. We use the PWIA, Eq. (16), to see the role of $\bar{\rho}_{K_B^A}$ clearly. The solid line in Fig. 3 shows the result of the PWIA without including the phase volume. More precisely, in this calculation $\bar{\rho}_{K_B^A}$ in Eq. (16) is replaced with

$$\bar{\rho}_0 \equiv \frac{\int \bar{\rho}_{K_B^A} dK_B^A}{\int_{\bar{\rho}_{K_B^A} \neq 0} dK_B^A}. \quad (23)$$

Then $d\sigma^{\text{PW}}/dK_B^A$ is just proportional to the effective s.p. MD of ^{14}O . As a result, the solid line in Fig. 3 has a purely symmetric shape with respect to its centroid momentum located at $P_{Bz}^A = 0$. If the phase volume $\bar{\rho}_{K_B^A}$ is taken into account as in Eq. (16), the dashed line is obtained. One sees that $\bar{\rho}_{K_B^A}$ gives a quite sharp cut of the PMD on the high momentum side. This results in the quite drastic shortening of the FWHM Γ , which is used as a measure of l . The result shown in Fig. 3 suggests that inclusion of $\bar{\rho}_{K_B^A}$, i.e., energy and momentum conservation, is necessary to relate the PMD and l properly. On the other hand, the peak height of the solid line is almost the same as that of the dashed line. The dotted line shows the result using

$$\bar{\rho}_{K_{Bz}^A}^{\text{av}} \equiv \frac{\int \bar{\rho}_{K_B^A} K_{Bb}^A dK_{Bb}^A}{\int_{\bar{\rho}_{K_B^A} \neq 0} K_{Bb}^A dK_{Bb}^A} \quad (24)$$

instead of $\bar{\rho}_{K_B^A}$ in Eq. (16). Although the shape of the dotted line is quite similar to that of the dashed line, the former

undershoots the latter at and below the centroid momentum (~ -80 MeV/c). Thus, accurate treatment of $\bar{\rho}_{K_B^A}$ is found to be important.

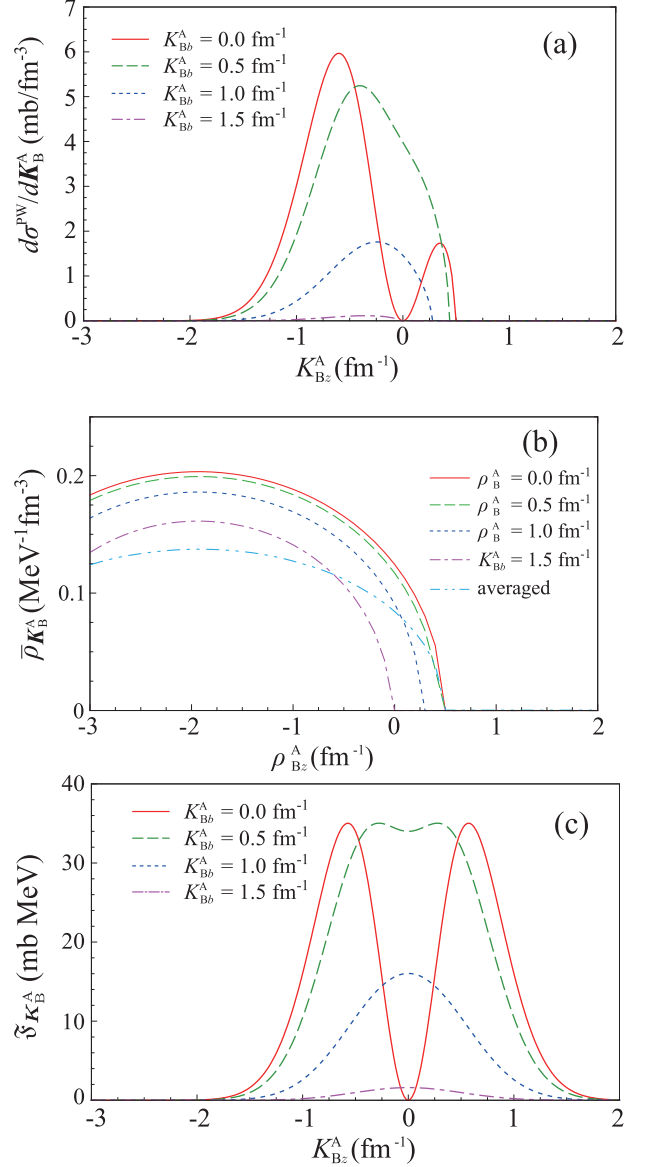


FIG. 4: (Color online) (a) Momentum distribution calculated with the PWIA, $d\sigma^{\text{PW}}/dK_B^A$, (b) phase volume $\bar{\rho}_{K_B^A}$, and (c) effective s.p. momentum distribution $\mathfrak{F}_{K_B^A}$, for the $^{14}\text{O}(p, pn)^{13}\text{O}$ reaction residue at 100 MeV/nucleon in inverse kinematics. The solid, dashed, dotted, and dash-dotted lines in each panel correspond to $K_{Bb}^A = 0.0, 0.5, 1.0,$ and 1.5 fm^{-1} , respectively. The dash-dot-dotted line in (b) shows the averaged phase volume $\bar{\rho}_{K_{Bz}^A}^{\text{av}}$.

The role of $\bar{\rho}_{K_B^A}$ is seen more clearly in Fig. 4. The MD $d\sigma^{\text{PW}}/dK_B^A$ is shown in Fig. 4(a) and decomposed into the phase volume $\bar{\rho}_{K_B^A}$ (Fig. 4(b)) and the effective s.p. MD $\mathfrak{F}_{K_B^A}$ (Fig. 4(c)). In each panel the solid, dashed, dotted, and dash-dotted lines correspond to $K_{Bb}^A = 0.0, 0.5, 1.0,$

and 1.5 fm^{-1} , respectively. As shown in Fig. 4(b), $\bar{\rho}_{\mathbf{K}_B^A}$ shows clear asymmetry with respect to $K_{Bz}^A = 0$. This behavior can easily be understood by its nonrelativistic expression. When $A \gg 1$, one finds from Eq. (20) that i) $\bar{\rho}_{\mathbf{K}_B^A}^{\text{NR}}$ has a maximum at $K_{Bz}^A = -K_0^A$ and ii) $\bar{\rho}_{\mathbf{K}_B^A}^{\text{NR}} = 0$ at $K_{Bz}^A = -K_0^A \pm [2(K_0^A)^2 - (K_{Bb}^A)^2 - \bar{S}_N]^{1/2}$. The phase volume $\bar{\rho}_{\mathbf{K}_B^A}$ plotted in Fig. 4(b), i.e., calculated with the relativistic kinematics, has the same features.

The effective s.p. MD at $K_{Bb}^A = 0$ shown by the solid line in Fig. 4(c) has a two peak structure and distributes up to $|K_{Bz}^A| \sim 2.0 \text{ fm}^{-1}$, reflecting the MD of the $0p3/2$ neutron inside ^{14}O . Since $\mathfrak{F}_{\mathbf{K}_B^A}$ is in fact independent of the direction of \mathbf{K}_B^A , the behavior of the other lines in Fig. 4(c) can be understood by that of the solid line. The MD of B is obtained by taking the product of $\bar{\rho}_{\mathbf{K}_B^A}$ and $\mathfrak{F}_{\mathbf{K}_B^A}$, which strongly suppresses the high momentum side, as shown in Fig. 4(a). One can find that the shape of the PMD (the dashed line in Fig. 3) is similar to the MD at $K_{Bb}^A = 0.5 \text{ fm}^{-1}$ (the dashed line in Fig. 4(a)). This is because the MD at around this value of K_{Bb}^A has the main contribution to the PMD. It should be noted that the averaged phase volume $\bar{\rho}_{\mathbf{K}_B^A}^{\text{av}}$ shown by the dash-dotted line in Fig. 4(b) quite well agrees with the dashed line for $K_{Bz}^A \gtrsim 0$, whereas the former undershoots the latter for $K_{Bz}^A \lesssim 0$. This explains the reason for the difference between the dashed and dotted lines in Fig. 3.

More intuitive interpretation of the role of $\bar{\rho}_{\mathbf{K}_B^A}$ can be given as follows. Let us consider two cases: 1) $\mathbf{K}_B^A = K_B^A \mathbf{e}_z$ and 2) $\mathbf{K}_B^A = -K_B^A \mathbf{e}_z$. Since B has the same energy in the two cases, $E_1^A + E_2^A$ is fixed at a same value because of the energy conservation. In a more rough estimation, the kinetic energy of B, T_B , is considered to be negligibly small. Then one finds

$$T_1^A + T_2^A \approx T_0^A - S_N. \quad (25)$$

On the other hand, the momentum conservation restricts the sum of K_{1z}^A and K_{2z}^A to be $-K_0^A - K_B^A$ in case 1) and $-K_0^A + K_B^A$ in case 2); note that $\mathbf{K}_0^A = -K_0^A \mathbf{e}_z$ in the A-rest frame. $|K_{1z}^A + K_{2z}^A|$ in the former is much larger than in the latter. Under the condition of Eq. (25), it is difficult to satisfy the momentum conservation in case 1).

When S_N is small, the cutoff momentum for $\bar{\rho}_{\mathbf{K}_B^A}$ becomes larger. In addition to that, the effective s.p. MD becomes narrower. These two make the effect of $\bar{\rho}_{\mathbf{K}_B^A}$ on the MD smaller. This is the reason for the difference in the PMD of ^{13}O (solid line) and ^{13}N (dashed line) on the high momentum side shown in Fig. 2. One can also expect a smaller effect of $\bar{\rho}_{\mathbf{K}_B^A}$ at higher incident energy. We will return to this point in Sec. III E.

D. Distortion effect on the low momentum side

One sees by comparing the solid line in Fig. 2 and the dashed line in Fig. 3 that the distortion generates a well-developed low momentum tail in the PMD. In the present eikonal DWIA model, as mentioned, the effect of distortion is

aggregated into the distorted-wave factor $F_{K_0 K_1 K_2}$; its form in inverse kinematics is given in Eq. (9). One sees from Eq. (9) that the imaginary part W_i of each optical potential gives a reduction of the amplitude of $F_{K_0 K_1 K_2}$, i.e., absorption. On the other hand, the real part V_i generates an effective momentum $\Delta \mathbf{K}_i$ for each particle; $\Delta \mathbf{K}_0$ is anti-parallel with the z -axis and $\Delta \mathbf{K}_1$ and $\Delta \mathbf{K}_2$ are parallel with the z -axis. One may interpret $\Delta \mathbf{K}_i$ as the momentum shift of a nucleon inside an attractive potential due to the local energy conservation.

Thus, the exponent $-iK_{Nz}z$ in Eq. (5) is effectively changed as

$$\begin{aligned} -iK_{Nz}z &\rightarrow -iK_{Nz}z + i(-\Delta K_0 + \Delta K_1 + \Delta K_2)z \\ &\approx i(K_{Bz}^A - \Delta K_0 + \Delta K_1 + \Delta K_2)z, \end{aligned} \quad (26)$$

where use has been made of $\mathbf{K}_N \approx -\mathbf{K}_B^A$. It is found that ΔK_0 is quite small because the kinetic energy of particle 0 is fixed at 100 MeV. On the other hand, particles 1 and 2 are allowed to have quite lower energies, for which the distortion effect is larger. Then K_{Bz}^A is effectively shifted toward the $+z$ direction by V_1 and V_2 . In other words, the PMD $d\sigma/dK_{Bz}^A$ probes the nucleon inside the nucleus A that has the longitudinal momentum around $|K_{Bz}^A + \Delta K_1 + \Delta K_2|$.

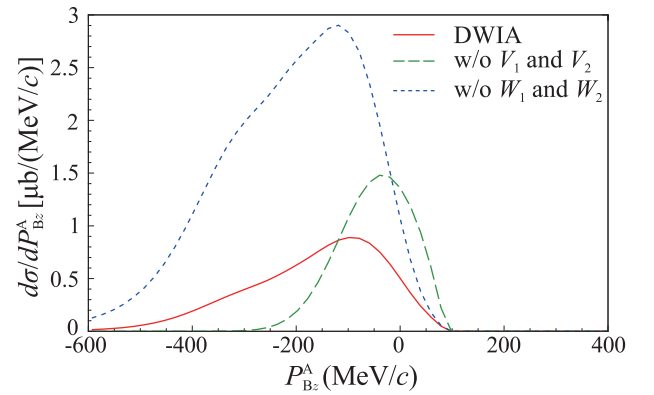


FIG. 5: (Color online) Parallel momentum distribution of ^{13}O for $^{14}\text{O}(p, pn)^{13}\text{O}$ at 100 MeV/nucleon in inverse kinematics. The solid line is the DWIA result, whereas the dashed (dotted) line represents the result calculated with $V_i = 0$ ($W_i = 0$) for particles 1 and 2.

To see this, we show in Fig. 5 the PMD of ^{13}O for $^{14}\text{O}(p, pn)^{13}\text{O}$ at 100 MeV/nucleon in inverse kinematics, calculated with the DWIA putting $V_i = 0$ (dashed line) and $W_i = 0$ (dotted line) for particles 1 and 2. For comparison we show by the solid line the DWIA result, which is the same as in Fig. 2. As clearly shown, V_1 and V_2 generate the low momentum tail. It should be remarked that the shift of the PMD towards the low momentum side by V_1 and V_2 affects also the height of the peak of the PMD. On the other hand, V_1 and V_2 change the integrated cross section by only about 5%.

In the actual calculation, as mentioned, the energy dependence of U_1 and U_2 is explicitly taken into account. It is found that the qualitative feature of the result shown in Fig. 5 does not change even if U_1 and U_2 are evaluated at a fixed energy, E_{fix} . Quantitatively, however, this treatment affects the result.

The height of the peak changes by about 60%, depending on the value of E_{fix} .

It is found that the momentum shift appears also in $^{14}\text{O}(p, 2p)^{13}\text{N}$ but the effect is quite small. This can be understood by the difference in S_N . Equation (25) shows that the kinetic energies of particles 1 and 2 are more severely restricted when S_N is large. Then the distortion effects due to V_1 and V_2 become more important.

E. Results at 200 MeV/nucleon

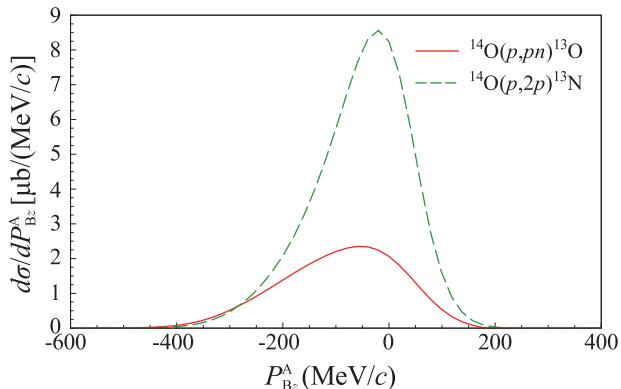


FIG. 6: (Color online) Same as Fig. 2 but at 200 MeV/nucleon.

Both the phase volume effect and the distortion effect discussed above will become less important as the incident energy increases. We show in Fig. 6 the PMD of the $^{14}\text{O}(p, pN)^{13}\text{O}$ at 200 MeV/nucleon. The meaning of the lines is the same as in Fig. 2. The two lines agree with each other around the tail on the high momentum side. This suggests that the phase volume effect becomes small, though not negligible. On the other hand, both results still show somewhat large asymmetry, i.e., A_Γ , indicating the importance of the distortion for particles 1 and 2 at this incident energy. The features of the results are summarized in Table II.

TABLE II: Same as Table I but at 200 MeV/nucleon; the result for $^{31}\text{Ne}(p, pn)^{30}\text{Ne}$ is also shown.

nucleus	P_{cen} (MeV/c)	Γ (MeV/c)	Γ_L (MeV/c)	Γ_H (MeV/c)	A_Γ
^{13}O	-53	278	168	110	1.53
^{13}N	-20	191	113	78	1.45
^{30}Ne	-0.7	52	32	30	1.08

When S_N is even smaller, the PMD becomes almost symmetric, as shown in Figure 7, in which the PMD of ^{30}Ne for $^{31}\text{Ne}(p, pn)^{30}\text{Ne}$ at 200 MeV/nucleon in inverse kinematics is plotted. We assume that the $1p3/2$ neutron with $S_N = 0.15$ MeV is knocked out. The most important feature of this reaction is that the $1p3/2$ neutron has a very narrow s.p. MD because of its small S_N . Within the range corresponding

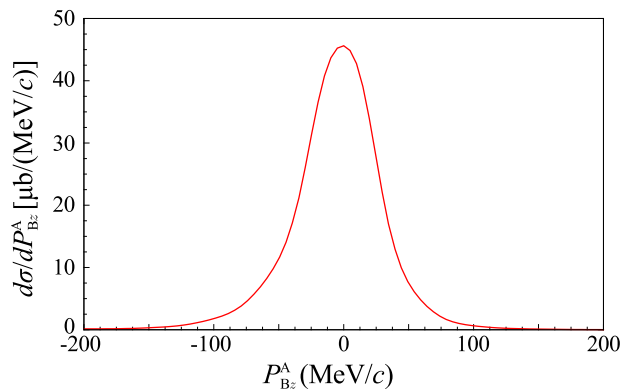


FIG. 7: (Color online) Same as Fig. 6 but for $^{31}\text{Ne}(p, pn)^{30}\text{Ne}$.

to the s.p. MD, K_{Bz}^A essentially gives no effect on the kinematics of the three-body system. In addition to that, since the $1p3/2$ neutron forms a halo, the main contribution to the reduced transition amplitude Eq. (5) comes from the surface region of the nucleus, which significantly suppresses the distortion effect. It should be noted that this is the case with only a very weakly-bound nucleus; for the $^{14}\text{O}(p, 2p)^{13}\text{O}$ process corresponding to a quite small value of S_N (4.63 MeV), the distortion effect still exists as shown in Fig. 6. The PMD for a knockout process of a very weakly-bound nucleon at around 200 MeV/nucleon shows, therefore, a symmetric shape rather exceptionally.

IV. SUMMARY

We have investigated the PMD of the residual nuclei of the $^{14}\text{O}(p, pn)^{13}\text{O}$ and $^{14}\text{O}(p, 2p)^{13}\text{N}$ reactions at 100 and 200 MeV/nucleon in inverse kinematics. An eikonal DWIA model was adopted, which was shown to reproduce the TDX data of the $^{12}\text{C}(p, 2p)^{11}\text{B}$ at 392 MeV very well. The PMD of both ^{13}O and ^{13}N have an asymmetric shape at 100 MeV/nucleon. The high momentum side steeply falls, whereas a well-developed tail exists on the low momentum side.

The former is found to be due to the phase volume effect reflecting the energy and momentum conservation. We have clarified how the phase volume affects the s.p. MD of the nucleon inside ^{14}O in detail by using PWIA. The width Γ of the PMD is much smaller than that of the s.p. MD by the phase volume effect. This should be remarked because Γ is used as a measure of the s.p. orbital angular momentum l . On the other hand, the phase volume does not change the peak height of the PMD. The phase volume effect becomes less important when S_N is small because 1) the cutoff momentum of the phase volume on the high momentum side is large and 2) the width of the s.p. MD is small.

The latter, the tail of the PMD on the low momentum side, is found to be due to the momentum shift of the outgoing two nucleons inside an attractive potential caused by the residual nucleus. Consequently, the PMD $d\sigma/dK_{Bz}^A$ probes the nu-

cleon inside the nucleus A having the longitudinal momentum $|K_{Bz}^A + \Delta K_{\text{eff}}|$, where $\Delta K_{\text{eff}} (> 0)$ is the effective momentum due to the distortion effect. It should be noted that ΔK_{eff} gives a somewhat large reduction of the peak height of the PMD, which is a key quantity to determine the spectroscopic factor \mathcal{S} . The momentum shift has a quite small effect ($\sim 5\%$) on the integrated cross section.

We found that at 200 MeV/nucleon the phase volume effect becomes less important, whereas the distortion effect still exists. For the $^{31}\text{Ne}(p, pn)^{30}\text{Ne}$ reaction at 200 MeV/nucleon, exceptionally, the PMD has an almost symmetric shape. This is because of the very small value (0.15 MeV) of S_N in this case. It should be remarked that the small distortion effect is due to the halo structure of ^{31}Ne ; the contribution of the nuclear interior region, where distorting potentials are large, to the (p, pN) transition amplitude is almost negligible.

For a quantitative comparison with experimental data of a PMD, on the low momentum side in particular, use of non-

eikonal scattering wave functions will be necessary. Extension of the present DWIA framework to knockout reactions by a nucleus will also be important for discussing various experimental data of nucleon removal processes measured so far.

Acknowledgments

The authors thank T. Noro for providing them with updated experimental data before publication. One of the authors (K.O.) thanks C. A. Bertulani and P. Capel for helpful discussions. This work was supported in part by Grant-in-Aid of the Japan Society for the Promotion of Science (Grant No. 25400255 and No. 15J01392) and by the ImPACT Program of the Council for Science, Technology and Innovation (Cabinet Office, Government of Japan).

-
- [1] I. Tanihata, H. Savajols, and R. Kanungo, *Prog. Part. Nucl. Phys.* **68**, 215 (2013).
- [2] J. H. Kelley *et al.*, *Phys. Rev. Lett.* **74**, 30 (1995).
- [3] A. Navin *et al.*, *Phys. Rev. Lett.* **81**, 5089 (1998).
- [4] F. Negoita *et al.*, *Phys. Rev. C* **59**, 2082 (1999).
- [5] E. Sauvan *et al.*, *Phys. Lett. B* **491**, 1 (2000).
- [6] V. Maddalena *et al.*, *Phys. Rev. C* **63**, 024613 (2001).
- [7] J. Enders *et al.*, *Phys. Rev. C* **65**, 034318 (2002).
- [8] D. Bazin *et al.*, *Phys. Rev. Lett.* **91**, 012501 (2003).
- [9] A. Gade *et al.*, *Phys. Rev. C* **69**, 034311 (2004).
- [10] E. Sauvan *et al.*, *Phys. Rev. C* **69**, 044603 (2004).
- [11] A. Gade *et al.*, *Phys. Rev. C* **71**, 051301(R) (2005).
- [12] A. Gade *et al.*, *Phys. Rev. C* **77**, 044306 (2008).
- [13] D. Bazin *et al.*, *Phys. Rev. Lett.* **102**, 232501 (2009).
- [14] G. F. Grinyer *et al.*, *Phys. Rev. C* **86**, 024315 (2012).
- [15] S. R. Stroberg *et al.*, *Phys. Rev. C* **90**, 034301 (2014).
- [16] J. A. Tostevin and A. Gade, *Phys. Rev. C* **90**, 057602 (2014).
- [17] R. J. Glauber, in *Lectures in Theoretical Physics* (Interscience, New York, 1959), Vol. 1, p.315.
- [18] M. S. Hussein and K. W. McVoy, *Nucl. Phys. A* **445**, 124 (1985).
- [19] K. Hencken, G. Bertsch, and H. Esbensen, *Phys. Rev. C* **54**, 3043 (1996).
- [20] J. A. Tostevin and B. A. Brown, *Phys. Rev. C* **74**, 064604 (2006).
- [21] M. Yahiro, K. Ogata, and K. Minomo, *Prog. Theor. Phys.* **126**, 167 (2011).
- [22] M. Kamimura, M. Yahiro, Y. Iseri, Y. Sakuragi, H. Kameyama, and M. Kawai, *Prog. Theor. Phys. Suppl.* **89**, 1 (1986).
- [23] N. Austern, Y. Iseri, M. Kamimura, M. Kawai, G. Rawitscher, and M. Yahiro, *Phys. Rep.* **154**, 125 (1987).
- [24] M. Yahiro, K. Ogata, T. Matsumoto, and K. Minomo, *Prog. Theor. Exp. Phys.* **2012**, 01A206 (2012).
- [25] K. Minomo, T. Matsumoto, K. Egashira, K. Ogata, and M. Yahiro, *Phys. Rev. C* **90**, 027601 (2014).
- [26] A. Bonaccorso and D. M. Brink, *Phys. Rev. C* **38**, 1776 (1988).
- [27] A. Bonaccorso and D. M. Brink, *Phys. Rev. C* **44**, 1559 (1991).
- [28] F. Flavigny, A. Obertelli, A. Bonaccorso, G. F. Grinyer, C. Louchart, L. Nalpas, and A. Signoracci, *Phys. Rev. Lett.* **108**, 252501 (2012).
- [29] D. Baye, P. Capel, and G. Goldstein, *Phys. Rev. Lett.* **95**, 082502 (2005).
- [30] G. Goldstein, D. Baye, and P. Capel, *Phys. Rev. C* **73**, 024602 (2006).
- [31] L. D. Faddeev, *Zh. Eksp. Theor. Fiz.* **39**, 1459 (1960) [*Sov. Phys. JETP* **12**, 1014 (1961)].
- [32] E. O. Alt, P. Grassberger, and W. Sandhas, *Nucl. Phys. B* **2**, 167 (1967).
- [33] T. Matsumoto, E. Hiyama, K. Ogata, Y. Iseri, M. Kamimura, S. Chiba, and M. Yahiro, *Phys. Rev. C* **70**, 061601(R) (2004).
- [34] T. Matsumoto, K. Katō, and M. Yahiro, *Phys. Rev. C* **82**, 051602 (2010).
- [35] M. Rodríguez-Gallardo, J. M. Arias, J. Gómez-Camacho, R. C. Johnson, A. M. Moro, I. J. Thompson, and J. A. Tostevin, *Phys. Rev. C* **77**, 064609 (2008).
- [36] M. Rodríguez-Gallardo, J. M. Arias, J. Gómez-Camacho, A. M. Moro, I. J. Thompson, and J. A. Tostevin, *Phys. Rev. C* **80**, 051601(R) (2009).
- [37] J. A. Tostevin *et al.*, *Phys. Rev. C* **66**, 024607 (2002).
- [38] G. Jacob and Th. A. J. Maris, *Rev. Mod. Phys.* **38**, 121 (1966).
- [39] G. Jacob and Th. A. J. Maris, *Rev. Mod. Phys.* **45**, 6 (1973).
- [40] P. Kitching, W. J. McDonald, Th. A. J. Maris, and C. A. Z. Vasconcellos, *Adv. Phys. Part. Nuclei* **15**, 43 (1985).
- [41] R. Crespo, A. Deltuva, E. Cravo, M. Rodríguez-Gallardo, and A. C. Fonseca, *Phys. Rev. C* **77**, 024601 (2008).
- [42] R. Crespo, A. Deltuva, and E. Cravo, *Phys. Rev. C* **90**, 044606 (2014).
- [43] Y. Kondo *et al.*, *Phys. Rev. C* **79**, 014602 (2009).
- [44] Y. Kondo *et al.*, *Phys. Lett. B* **690**, 245 (2010).
- [45] A. Ozawa *et al.*, *Phys. Rev. C* **84**, 064315 (2011).
- [46] T. Noro *et al.*, *J. Phys. Conf. Ser.* **20**, 101 (2005); T. Noro, private communication (2014).
- [47] T. Aumann, C. A. Bertulani, and J. Ryckebusch, *Phys. Rev. C* **88**, 064610 (2013).
- [48] N. S. Chant and P. G. Roos, *Phys. Rev. C* **15**, 57 (1977).
- [49] A. Bohr and B. R. Mottelson, *Nuclear Structure* (Benjamin, New York, 1969), Vol. I.
- [50] A. J. Koning and J. P. Delaroche, *Nucl. Phys. A* **713**, 231 (2003).
- [51] S. Hama, B. C. Clark, E. D. Cooper, H. S. Sherif, and R. L. Mer-

- cer, Phys. Rev. C **41** 2737 (1990) ;
E. D. Cooper, S. Hama, B. C. Clark, and R. L. Mercer, *ibid.* **47**,
297 (1993).
- [52] G. Perey and B. Buck, Nucl. Phys. **32**, 353 (1962).
- [53] M. A. Franey and W. G. Love, Phys. Rev. C **31**, 488 (1985).
- [54] G. van der Steenhoven *et al.*, Nucl. Phys. A **480**, 547 (1988).